ORIGINAL PAPER

Influence of cerium concentration on the structure and properties of silica-methacrylate sol–gel coatings

Nataly Carolina Rosero-Navarro · Pawel Figiel · Roman Jedrzejewski · Anna Biedunkiewicz · Yolanda Castro · Mario Aparicio · Sergio Antonio Pellice · Alicia Durán

Abstract The aim of this work was to study the effect of the incorporation of cerium nitrate in a silica-methacrylate sol–gel hybrid matrix reinforced with silica nanoparticles. Sols, coatings and powders have been studied, focusing specially in the determination of the redox ratio Ce^{3+}/Ce^{4+} and films structure. Sols have been characterised using viscosity measurements and FT-IR spectroscopy, and powders and coatings obtained with different Ce contents through UV–Vis and FT-IR spectroscopy, TGA, TEM, AFM and FE-SEM. The goal was to reach the best compromise between maximum cerium concentration and coating stability to better understand the mechanisms acting in active anti-corrosive processes.

Keywords Hybrid coating · Film structure · Redox ratio Ce^{3+}/Ce^{4+} · Inhibition behaviour

1 Introduction

AA2024 is the most common aluminium alloy used in aerospace industry for numerous applications, due to its suitable strength to weight ratio, good damage tolerance

N. C. Rosero-Navarro (✉) · Y. Castro · M. Aparicio · S. A. Pellice · A. Durán
Instituto de Cerámica y Vidrio (CSIC), Madrid, Spain
e-mail: karolrosero@icv.csic.es

P. Figiel · R. Jedrzejewski · A. Biedunkiewicz
West Pomeranian University of Technology, Institute of Materials Science and Engineering, Szczecin, Poland

Present Address:
S. A. Pellice
Instituto de Investigaciones en Ciencia y Tecnología de Materiales (CONICET), Mar del Plata, Argentina

and low cost. In this alloy, a heterogeneous microstructure is intentionally developed by addition of copper to increase mechanical properties. Thus, any treatment to improve the corrosion resistance of AA2024 should not rise above 120 °C to avoid dissolution of the intermetallic particles. At present, the most efficient protection systems are chromium based coatings, like Chromium Conversion Coatings (CCC) and Chromium Acid Anodised (CAA), which offer a self-healing protection. However, the toxicity and carcinogenic properties of the hexavalent chromium ion have caused severe restrictions to be imposed on its use by international environmental standards [1].

The sol–gel method provides an alternative to chromium based systems because it usually presents a low environmental impact, and the incorporation of different secondary phases including metal, organic monomers and inorganic nanoparticles allows obtaining materials with the desired properties as density and hydrophilic character. Thus, it is possible to obtain hybrid organic–inorganic sol gel coatings cured at low temperature and able to preserve the integrity of the metallic substrate and to diminish the risk of appearance of cracks or defects [2]. The preparation of hybrid structures needs a rigorous control of all parameters involved in the synthesis to obtain a homogeneous interpenetration of both networks without phase separation. Organically modified silicon alkoxides with organic polymerisable groups attached to the silicon atom are now available. Most published papers [3–6] exploit a strategy based on epoxy groups attached to silicon to promote the synthesis of the organic network. Different aluminium alloys have been coated with epoxy and methacrylate based sol–gel coatings [3–9] treated with sintering temperatures below 200 °C. These coatings present good barrier properties, which hinder the penetration of the electrolyte towards the metallic substrate, but degradation is observed

at long immersion times as a consequence of the water uptake.

Alternatively, different research works deal with the incorporation of inhibitors to the sol–gel matrix, to improve its corrosion resistance obtaining a system with active protection [8–15]. The selection of new inhibiting compounds is made according to the principles of green chemistry [16]. Most publications are focused on the use of rare-earth metal compounds as alternative to chromates. Among them, cerium salts have shown to provide protection for aluminium alloys against corrosion [8–12, 17–19]. The protection mechanism proposed consists on the deposition of mixed cerium (III and IV) hydroxides/oxides on cathodic areas triggered by an increase of pH. Although they are clear signals indicating that cerium participates in the self-healing and corrosion protection process, most papers also show the degradation of coating structure with cerium incorporation [8–12]. In previous works [8, 9], we have confirmed that cerium induces a porous structure in methacrylate base coatings diminishing the barrier properties of the layers respecting to those without cerium.

On the other hand, the incorporation of cerium has been widely studied [20–27] as dopant in silicate glasses prepared by melting or sol–gel process, for applications as phosphors, scintillators, detectors, UV absorbers, emitters and activators due to its luminescence properties. Cerium presents two valence states, ceric (Ce^{4+}) and cerous (Ce^{3+}); the electronic configuration of the element corresponding to $[Xe]\ 4f^1\ 5d^1\ 6\ s^2$. The optical absorptions of both valence states of cerium appear in the UV region presenting two different symmetries, octahedral (coordination number $= 6$) and dodecahedral (coordination number $= 8$) [28, 29]. For Ce-doped silicate glasses obtained by melting at temperatures above 1,400 °C, the UV spectra show two mains peaks: one at 240–250 nm, assigned to a Ce^{4+} charge transfer, and other around 310–320 nm due to the electronic transition [21–24] $4f \rightarrow 5d$ of Ce^{3+}. The simultaneous presence of Ce^{3+} and Ce^{4+} produces a strong optical absorbance mainly caused by the intense Ce^{4+} absorption band, permitted by Laporte rule [25, 29]. The optical absorptions of ceric and cerous ions in Ce-doped silica coatings produced by sol–gel appear at similar wavelengths that in Ce-doped silicate glasses prepared by melting [28, 30, 32]. However, these bands can shift to greater or shorter wavelengths due to thermal treatments, water chemical bond and contra-ions presence [26–32].

From the corrosion protection perspective using hybrid sol–gel coatings, it is interesting to elucidate the redox behaviour of cerium in the coatings and its effect in the structure of the hybrid coating matrix, to shed light on the protective mechanisms taking place during corrosion process and, consequently, the release capacity of the inhibitor to participate in the active protecting process.

The effect of the incorporation of cerium nitrate in a silica-methacrylate sol–gel hybrid matrix reinforced with colloidal silica nanoparticles has been studied. Sols, coatings and powders were analysed, focusing especially in the determination of the redox ratio Ce^{3+}/Ce^{4+} and on the film structure. The goal is to reach the best compromise between maximum cerium concentration and coating stability to better understand the mechanism acting in active anti-corrosive processes. The hybrid organic–inorganic matrix was obtained from the hydrolytic condensation of tetraethoxysilane (TEOS) and 3-methacryloxypropyl trimethoxysilane (MPS), which has a free-radical polymerisable C=C double bond. A bifunctional monomer, ethylenglycol-dimethacrylate (EGDMA) with two C=C double bonds, was used to develop a highly crosslinked organic network attached to the inorganic one through covalent Si–C bonds. Sols have been characterised using viscosity measurements and FT-IR spectroscopy, and powders and coatings obtained with the different compositions through profilometry, contact angle, UV–Vis spectroscopy, FT-IR spectroscopy, TGA, TEM, AFM and FE-SEM.

2 Experimental

A series of hybrid organic–inorganic sols were prepared from tetraethoxysilane (TEOS, ABCR 98%), 3-(methacryloxypropyl)trimethoxysilane (MPS, ABCR 98%), ethyleneglycol-dimethacrylate (EGDMA), silica nanoparticles (Levasil 200A, Bayer, aqueous suspension 40 wt%, particle size 20 nm, pH 9) and cerium nitrate ($Ce(NO_3)_3\cdot6H_2O$, Aldrich, 99%) as source of Ce(III). 2,2′-azobis(isobutyronitrile) (AIBN, Aldrich, 98%) was used as initiator of the free-radicals organic polymerisation. The sol is called TME-SiO_2 here in after.

Hydrolysis and condensation reactions of TEOS and MPS were produced in presence of silica nanoparticles and organic crosslinker (EGDMA) after concentrated HNO_3 acid was added (0.6 vol%). A spontaneous destabilization of the basic silica suspension takes place allowing a fast grafting of the silica nanoparticles surface through the condensation of hydrolyzed TEOS and MPS molecules. This process was described in detail in a previous article [7]. TME-SiO_2 sol was prepared keeping the molar ratio 62.5 TEOS: 25 MPS: 12.5 EGDMA; colloidal silica suspension was added in a ratio of 35 mol % respect to alkoxides. The final pH of the sol was around 2.

The resulting TME-SiO_2 sol was doped with 1, 3, 5, 7 and 9 mol % of $Ce(NO_3)_3\cdot6H_2O$, respect to the alkoxides by directly adding the suitable amounts of Ce salt to the final precursor sol. The doped sols are denoted as

TME-SiO$_2$-xCe, where x represents the mol % of cerium nitrate. Sols were kept at 4 °C and protected of the solar light by maintaining in amber bottles along different ageing periods up to a maximum of 300 h standstill.

The rheological characterisation of sols was followed by measuring the viscosity as a function of ageing time using a rotational rheometer (Haake, RS50, Germany) with a cone-plate fixture (5 mL sample). Measurements were performed at 25 °C and the shear rate was increased, in 3 min, from 0 to 600 s^{-1}, kept for 1 min at the maximum rate and decreased to 0 s^{-1} at the same speed.

Glass slides (2.5 × 7 cm^2) were coated with TME-SiO$_2$ and TME-SiO$_2$-xCe sols with different ageing times and varying the withdrawal rates between 4 and 20 cm/min. Coatings were dried at room temperature and cured at 60 °C for 10 h with a further treatment in air at 120 °C for 2 h with a heating rate of 10 °C/min to promote organic polymerisation.

Powdered samples were also prepared from gels with the same thermal treatment, their density being determined by pycnometry. Moreover, the gel powders were subjected to thermo-gravimetric analysis (SDT Q600 TA Instruments) in air atmosphere with flow of 100 mL/min, in non-isothermal condition, with mass samples of 20 ± 2 mg and constant heating rate (20 °C/min).

Fourier Transform Infrared Spectroscopy by Attenuated Total Reflectance (ATR-FTIR, Perkin Elmer, Spectrum 100) was used to study the effect of the cerium content on the chemical structure and polymerisation of sols and coatings. FTIR spectra were recorded between 650 and 4,000 cm^{-1}, with a resolution of 2 cm^{-1}. Spectra were deconvoluted using PeakFit software considering Gaussians and Lorentzian bands. Residual root mean square (RMS) errors were around 0.001.

Ultraviolet–Visible spectra (UV–Vis, Perkin Elmer, Lambda 950) of coatings and powdered samples were recorded with an Integrated Sphere in Reflectance mode and further converted in absorption through Kubelka–Munk equation. The baseline was recorded with non doped materials as reference. Ce^{3+}/Ce^{4+} ratio was determined as a function of Ce content after deconvolution using Peak-Fit.

The coating thickness was measured by profilometry (Talystep, Taylor Hobson, UK) and the contact angle of distilled water on the films was measured with an Easy Drop Krup equipment using the Young–Laplace Method through Sessile Drop Fitting software.

Coatings were also studied by optical microscopy (Zeiss, HP1, Germany), Field Emission Scanning Electron Microscopy (FE-SEM, HITACHI S-4700) and Atomic Force Microscopy (AFM, NanoScope IVa, Veeco). Powders and coatings were analysed by Transmission Electron Microscopy (TEM, Hitachi H-7100, Japan).
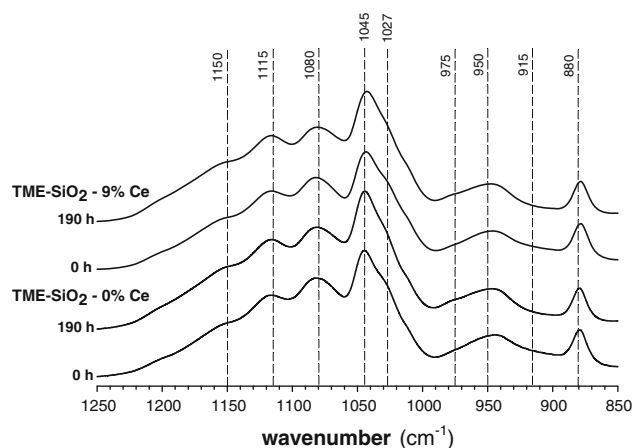
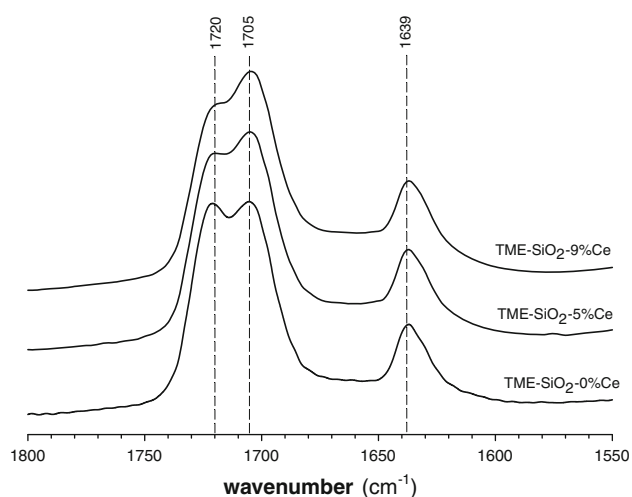# 3 Results and discussion

3.1 Characterisation of the sols

TME-SiO$_2$ hybrid organic–inorganic sol, obtained from hydrolysis and condensation of TEOS and MPS in presence of an organic crosslinker (EGDMA) and silica nanoparticles was transparent and colourless. The addition of cerium salt did change the aspect of the sols to slightly yellow, all of them presenting excellent wettability behaviour on glass slides substrates.

Since the hydrolytic condensation is advanced almost completely after the synthesis of the TME-SiO$_2$ sol [7], the addition of the corresponding amounts of hexa-hydrated cerium nitrate does not produce additional changes in the evolution of the Si–O–Si bonds. In fact, since water supplied by the silica nanoparticle suspension is nearly the stoichiometric needed to complete hydrolytic condensation; the excess of water supplied by the cerium salt was not consumed in the further condensation process carried out during the ageing period.

Figure 1 presents the FTIR spectra of TME-SiO$_2$ and TME-SiO$_2$-9Ce sols just prepared and after 190 h of ageing, pointing out the main bands related to the hydrolysis and condensation. At the starting moment all the bands corresponding to the asymmetric vibration of the Si–O–Si bond [7, 33], at 1,150, 1,115, 1,080 and 1,045 cm^{-1}, are clearly developed confirming the quasi instantaneous character of these reactions. After 190 h of ageing all these bands, excepting that at 1,080 cm^{-1}, assigned to Si–O–Si bonds in dense silica nanoparticles, experience a slight but evident growing confirming the advance of the condensation process. The bands corresponding to non-bridging oxygen, Si–OH groups [33, 34], at 975 and 950 cm^{-1}, and Si–O$^-$ fragments [35], at 915 cm^{-1}, show slight diminutions correlated to the advance of the silica condensation.

Fig. 1 TME-SiO$_2$ and TME-SiO$_2$-9Ce sols just prepared and after 190 h aging

Fig. 2 TME-SiO$_2$, TME-SiO$_2$-5Ce and TME-SiO$_2$-9Ce sol just prepared

Alcohols produced during hydrolysis of alkoxides are detected through the bands of ethanol, at 1,088 and 1,045 cm^{-1}, both overlapped with the silica bands, and methanol, at 1,027 cm^{-1}, with slight changes during the ageing process. Additionally, Fig. 2 shows the FTIR spectra of three sols between 1,880 and 1,550 cm^{-1}. In this region it is possible study the evolution of vibration groups corresponding to C=O and C=C present in the structure and coming from EGDMA and MPS, organic and hybrid precursors. The band at 1,639 cm^{-1} is assigned to C=C, while C=O band presents three different components[34]: a band at 1,705 cm^{-1}, assigned to C=O hydrogen bonded to OH groups of EGDMA or to Si–OH groups generated in the first stage, other at 1,720 cm^{-1}, assigned to C=O stretching vibrations that are conjugated to C=C double bonds, and a band at 1,732 cm^{-1}, assigned to C=O stretching vibrations, produced during the organic polymerisation and not conjugated to C=C double bonds. The incorporation of cerium salt in the sols produces a change in the relative intensity of the C=O absorption at 1,705 cm^{-1}, that could be caused by

the formation of hydrogen bonds developed between C=O and the excess of water added with the hexa-hydrated Ce salt, and/or with cerium ions. This last aspect will be discussed in detail in a following section through the UV–Vis optical spectra in coatings and powders. This study was not possible to perform in the liquid sols because the high concentration of cerium produced the saturation of the spectra.
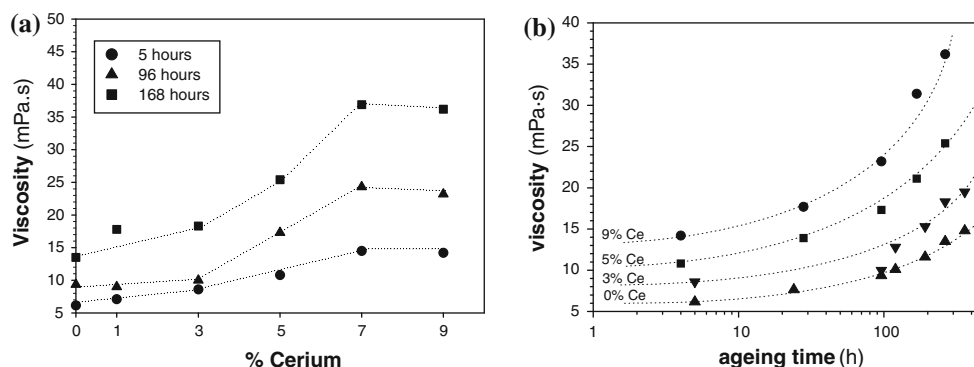
The cerium incorporation provokes a clear effect in the viscosity of the sols. Figure 3a shows the evolution of viscosity with cerium content, showing a strong increase for concentrations higher than 5% up to 7%; a further increase of Ce up to 9% does not produce additional increment of viscosity, likely indicating the precipitation of cerium compounds. On the other hand, as sols are aged, viscosity rises exponentially in a logarithmic scale of time, Fig. 3b. Even after 300 h all the sols presented Newtonian behaviour.
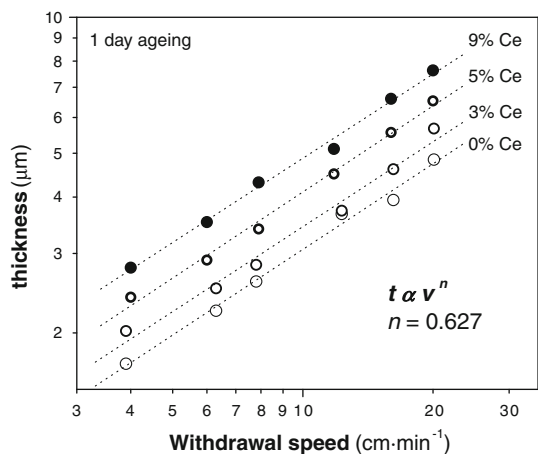
3.2 Characterisation of the coatings

Monolayer coatings with thickness between 2 and 12 μm were obtained by dipping. All of them were highly adherent and crack-free after the thermal treatment. A yellowish coloration was developed accordingly the Ce content increased. Non-doped sols produced colourless coatings. Figure 4 shows the evolution of the coating thickness with the withdrawal rate for Ce doped sols with 24 h of ageing. Coating thickness (*t*) is related with to withdrawal rate (*v*) by the expression:

$$t_s = 10^{-3} J (\eta v / \rho g)^n (C / \rho_s)$$

were *C* is a concentration sol, ρ_y ρ_s are the sol and coating densities, η the viscosity of the sol and *J* is a un-dimensional flow constant. The theoretical value [36, 37] of the exponent in inorganic sol–gel coatings is 0.5. In this case, the exponent *n* was near constant, around 0.62, and independent of the Ce content. Deviations from the theoretical value are attributed to modification of the rheological and

Fig. 3 Viscosity of the sols as a function of the Ce content (**a**); and ageing time (**b**)

Fig. 4 Coating thickness as a function of the withdrawal speed for sols with different Ce contents

Fig. 5 Contact angle of TME–SiO$_2$–x Ce coatings as a function of the cerium content

flowing behaviour of the hybrid sols by the presence of organic components and silica nanoparticles which could also affect the densification process [38].
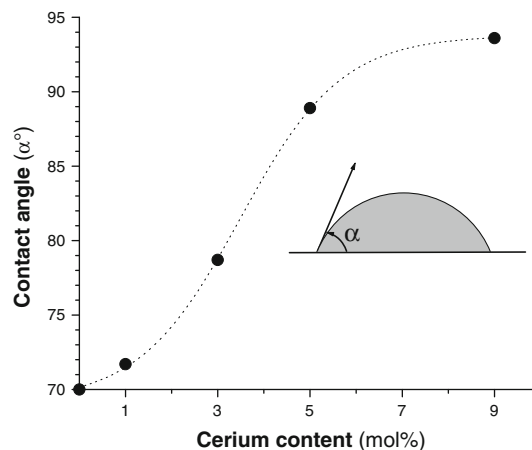
The increment of viscosity due to increasing cerium content and/or over-condensation produced during the ageing of sols, leads to a growing of the coating thickness.

Thicker coatings and greater cerium contents could be suitable to provide self-healing effect also enhancing the barrier properties when deposited onto metallic alloys. However, slight cloudiness was observed in coatings obtained from sols with 3% Ce aged during 260 h and sols with higher Ce contents aged for 100 h. This effect is visually observed in thicker coatings, likely produced by phase separation, observed as a cellular structure through optical microscopy (not shown).

Since anticorrosive coatings are usually covered by water based polymeric paints, used as protective and aesthetic finishing, the surface wettability plays an important role. Contact angle of water increased with Ce doping from near 70° for non-doped coatings, up to reach a maximum angle of 94° for 9% Ce, Fig. 5. This strong diminution of wettability of Ce doped coatings may represent a problem for the adhesion of the final protective to coat that should be solved. Although the chemical nature of a solid surface has a main influence on its wetting behaviour, the morphological structure could also induce important changes [39, 40]. The experimentally measured contact angle (θ_0) is related with the intrinsic one (θ_e) by the Wenzel's equation:

$$\cos \theta_e = r \cdot \cos \theta_0$$

where r is a roughness factor. Thus, the higher the roughness, the higher should be the contact angle θ_0. This explanation is further supported by AFM measurements.

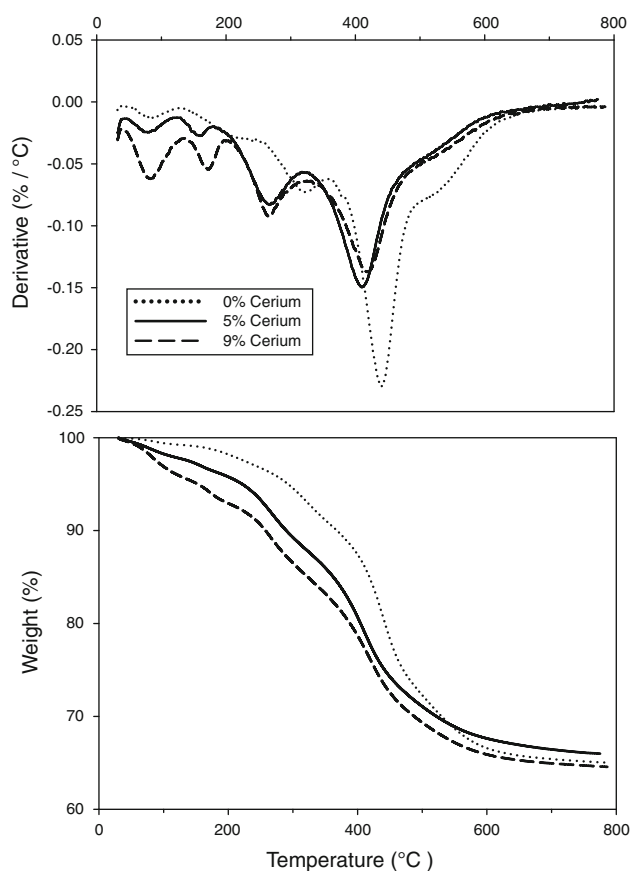## 3.3 Structure of coatings and powders

The structure and evolution of Ce-containing coatings and powders were studied through density, TGA, FTIR, TEM, AFM and FE-SEM. The powder analysis is included to compare the different final structures of coatings and bulk materials from same sols.

As expected, a linear rising of density is observed for increasing Ce contents, changing from 1.55 to 1.70 g/cm^3 for 0 to 9% Ce-containing powders (no shown).

Mass change curves (TG) and their derivates (DTG) permit to follow the evolution of powder samples with heat treatment, Fig. 6. Different losses are identified in all the samples at similar temperature ranges. The weight loss below 100 °C is assigned to adsorbed water in samples, being higher as higher is the Ce content. The mass loosening between 150 and 200 °C can be explained as the release of water produced by the further reaction of Si–OH groups; while at higher temperature, between 250 and 300 °C, O–CH$_2$CH$_3$ and O–CH$_3$ residual groups are involved in the condensation process with the consequent release of ethanol and methanol [41]. The strong weight losses observed between 330 and 500 °C can be attributed to the thermal degradation and final combustion of the organic compounds.

It is observed that all the thermal events occur at lower temperatures when Ce content increases, excepting the releasing of adsorbed water. This fact could be related to the generation of a less dense (or more porous) structure as a consequence of Ce doping. Besides the water excess carried by the cerium salt (hexahydrated nitrate), cerium doping could catalyze the hydrolytic condensation generating a further amount of water resulting in a more open structure, and producing a higher release at temperatures below 100 °C.

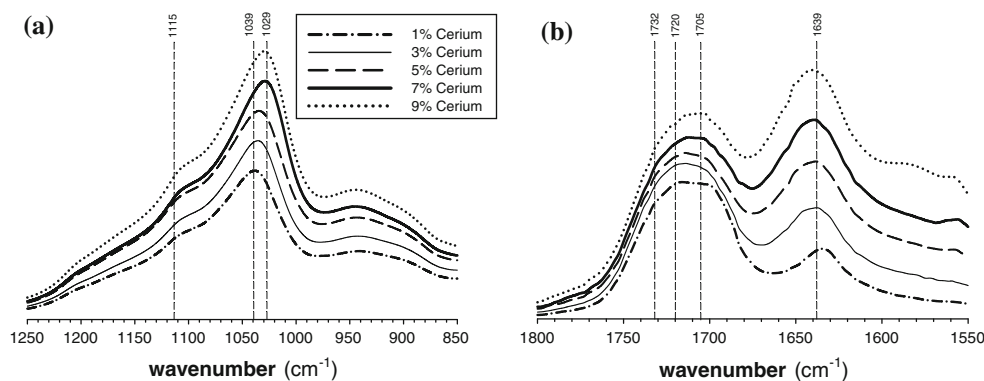**Fig. 6** TG and DTG curves of powdered samples containing 0, 5 and 9% of Ce

Changes in silica structure can be analysed through the behaviour of the Longitudinal Optic (LO) and Transversal Optic (TO) components of the asymmetric vibration of the Si–O–Si bond in the infrared spectra. Almeida et al. found that the gel pores may account for the activation of the LO component [42]. Thus, the presence of second phases or organic compounds in a sol–gel silica network can induce both porosity and lower strains on the Si–O–Si bond, which reflect on a shift of the TO component to lower wavenumbers [38, 43]. Figure 7a presents the FTIR spectra of

Ce-containing coatings; a clear trend is observed on the position of the TO band, moving from 1,039 to 1,029 cm^{-1} when Ce increases from 1 to 9%, indicating some stress relaxation of the silica network. The frequency of Si–O–Si bands of colloidal silica at 1,080 cm^{-1} is overlapped with the main Si–O–Si band. Moreover, LO Si–O–Si band around 1,115 cm^{-1} is present in all the spectra, slightly growing for Ce contents higher than 5% indicating the evolution of coating porosity with Ce amount.
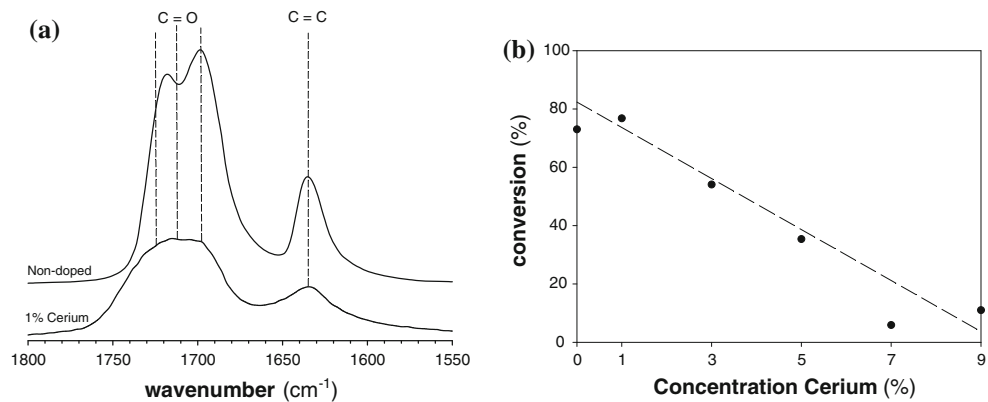
On the other hand, the thermal treatment of coatings at 60 °C produces the free radical polymerisation of the C=C double bonds through the thermal decomposition of AIBN. The increase of the cross-linking is a key factor to obtain more dense, homogeneous and mechanical resistant coatings. The decrease of the C=C band at 1,639 cm^{-1} is a sign of the advance of polymerisation. The lower the cerium concentration, the lower is the intensity of the C=C band at 1,639 cm^{-1}, Fig. 7b.

Figure 8a shows the FTIR spectra between 1,880 and 1,550 cm^{-1} of non-doped (C=C initial concentration) and 1% Ce doped coatings. The C=O bands shift to larger wavenumbers when organic polymerisation develops. Moreover, the addition of cerium induces a further change in the relative intensity of C=O bands as observed in paragraph 3.1. Thus, C=O bands are not appropriate references for a rigorous quantitative evaluation of the conversion of C=C bands. However, for taking an approach to the polymerisation degree we have calculated the C=C conversion as the ratio of the areas of C=C cerium doped coatings bands related with that of non doped and non polymerised coating, using as normalisation reference the total area of C=O bands for each Ce concentration, Fig. 8b. The conversion of C=C groups shows an inversely proportional dependence between polymerisation degree and cerium content, moving from around 80% for un-doped coats down to values about 10% for 9% cerium content. This behaviour could be explained taking into account the steric hindrance introduced by cerium bonds in the coatings that diminishes the probability of polymerisation. Some authors report the role of cerium as catalyst of hydrolytic

Fig. 7 FTIR absorbance spectra of Ce containing coatings

Fig. 8 a FTIR absorbance spectra of coatings TME-SiO$_2$-1Ce compared with TME-SiO$_2$ without thermal treatment, and b C=C conversion as a function of Ce content

condensation, this being a further explanation of this steric impediment for organic polymerisation.

The structure of coatings and powders has been also studied by TEM, FE-SEM and AFM. Electronic microscopy (TEM and FE-SEM) showed the presence of Ce containing nanoparticles with a narrow size distribution, around 20 nm in diameter, for Ce contents higher than 3%. Figure 9 shows TEM images of graphite replicas obtained from coatings with 3 and 9% mol of Ce. Microphotographs (c) and (d) were obtained through magnification of agglomerates shown in (a) and (b), respectively, showing that the elemental nanoparticles present a homogeneous size around 20 nm, while the agglomerates have a medium size of 800–1,000 nm.

EDS analysis revealed that these particles are composed by amorphous Ce$_x$O$_y$. Nanometric Ce$_x$O$_y$ agglomerates were also observed by FE-SEM in cross-section of Ce-coatings confirming the precipitation of cerium compounds, Fig. 10. A similar behaviour, with higher precipitates, was observed in powders samples (not shown).

Additionally, Fig. 11 depicts the topographic AFM images obtained from coatings with different amounts of cerium. When Ce content increases, roughness progressively raises, from 6 nm for non-doped coatings, to 7 nm for 1% mol Ce, 9 nm for 5% mol Ce and 15 nm for 9% mol Ce. The development of roughness, explained by superficial agglomeration/precipitation of cerium containing nanoparticles, confirms data obtained by TEM.
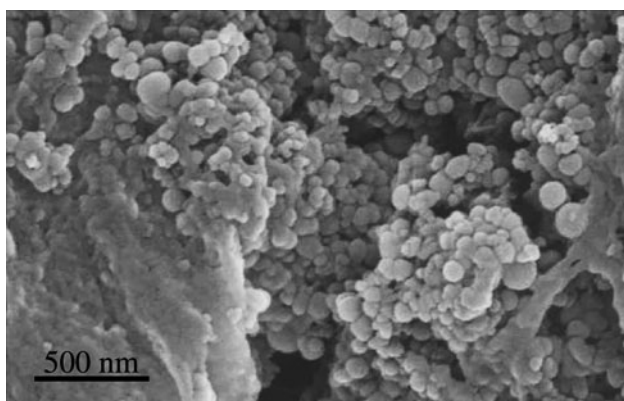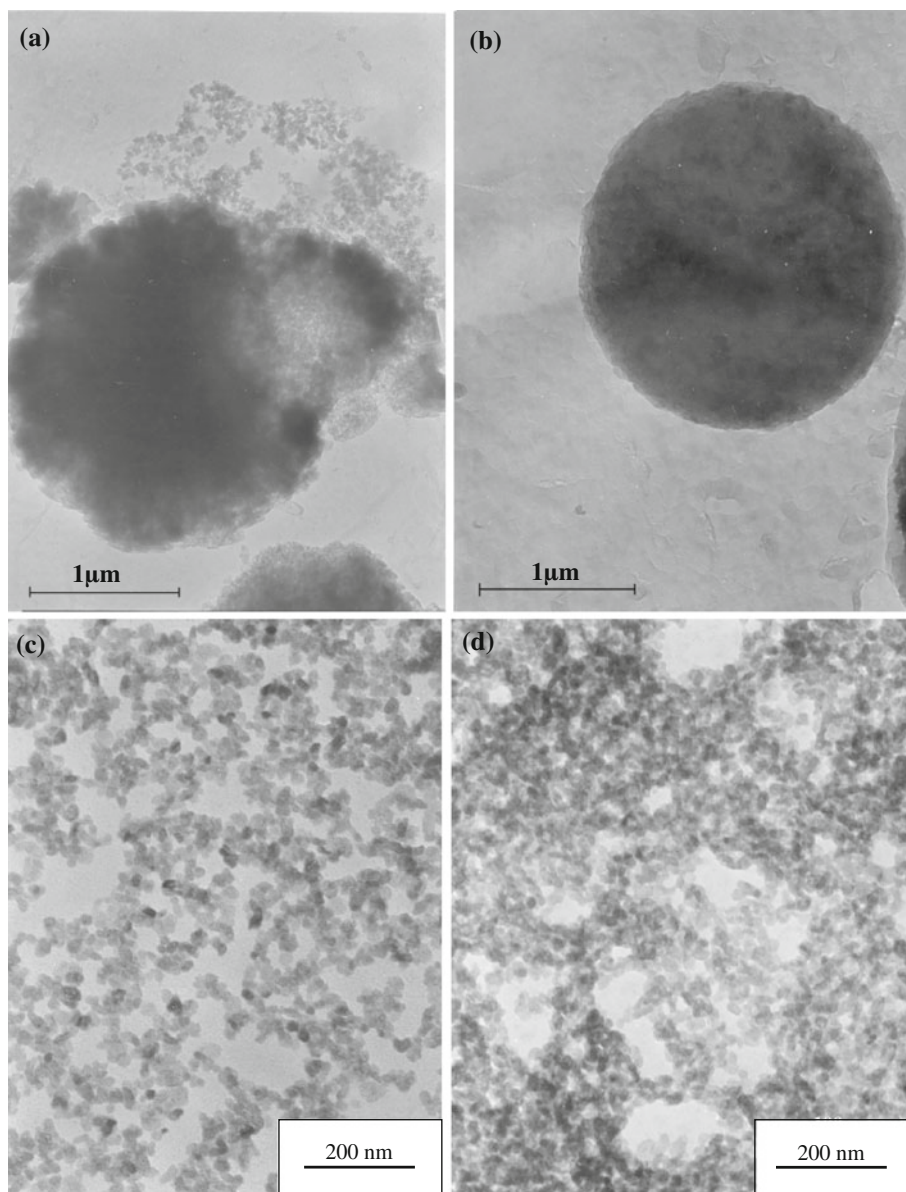
3.4 Redox behaviour of Ce in coatings and powders

UV–Visible spectra were recorded to study the redox behaviour of cerium in coatings and powders. UV–Visible spectra of Ce-doped coatings normalized by the coating thickness are presented in Fig. 12 along with the spectra of powder samples. According to literature, UV–Visible spectra of cerium in silicate glasses and coatings [21–32], show two main bands, one centred around 240–250 nm, assigned to a charge transfer between Ce^{4+} and a ligand oxygen, and the other around 310–320 nm due to the electronic transition [21–24] 4f → 5d of Ce^{3+}.

Ce-doped coatings (Fig. 12a) present a wide band centred around 320 nm corresponding to the trivalent state. The band is highly asymmetric, its maximum shifting to longer wavelength with increasing cerium contents. On the other hand, Ce-doped powders (Fig. 12b) show more complex bands with different contributions, mainly at 280 nm and 320 nm assigned to the presence of both, Ce^{4+} and Ce^{3+}. These results reveal a partial oxidation of Ce^{3+} to Ce^{4+} in powders, not appearing in the coatings obtained from the same sols.

Deconvolution of UV–Visible spectra of cerium doped coatings and powders were developed to better understand the evolution of the spectral components of the bands. Although the deconvolutions were performed on spectra plotted as a function of wavenumber, wavelengths are used for the discussion to facilitate the comparing with literature data.

Figure 13a shows the deconvolution of TME-SiO$_2$-5Ce coating spectrum and Fig. 13b illustrates the evolution of the absorption bands as a function of cerium concentration. UV–Visible spectra for all cerium concentrations can be fitted with two bands. The first one is centred at 310 nm, its wavelength shifting from 304 to 315 nm with increasing cerium concentration. The second band is centred at 335 nm no shifting being appreciated for any cerium content. The asymmetry of the band of Ce^{3+} can be associated to the energy shift of the 4f-5d transition and its nephelauxetic effect, used for explaining the behaviour of the Ce^{3+} and rare earth ions in silica glass matrix [23, 32]. As mentioned previously the introduction of cerium ions in the hybrid structure could generate new complexes and different nearest neighbour arrangements with oxygens, and probably OH groups coming from organic/inorganic precursors. The chemical nature of the neighbours determines the electrical field sensed by d orbitals; so that, energy splitting will be likely produced and bands wavelength will be highly affected. Since Ce^{3+} presents a 5d$_5$ electric structure, the energy of d orbitals will easily change with the distortion of neighbour arrangements, explaining the splitting of the absorption at 315 nm in two

Fig. 9 TEM images of graphite replica obtained from coatings. **a, c** TME-SiO$_2$-3Ce and **b, d** TME-SiO$_2$-9Ce
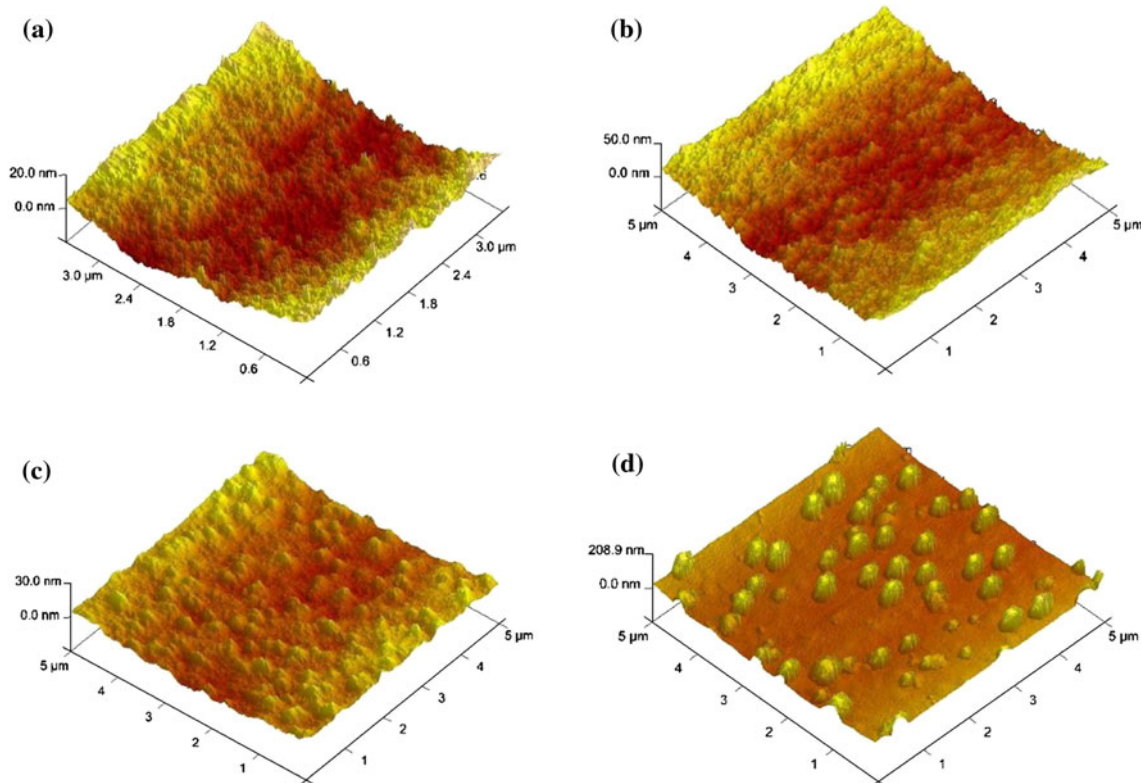

Fig. 10 FE-SEM micrograph of a TME-SiO$_2$-3Ce coating

bands. In silicate glasses only one band at 310–320 nm is reported for Ce^{3+}, but this is usually asymmetric and could be deconvoluted in two bands in most cases. For example, silica glasses doped with Al and P show shifting of Ce^{3+} band and splitting of d orbitals [32].
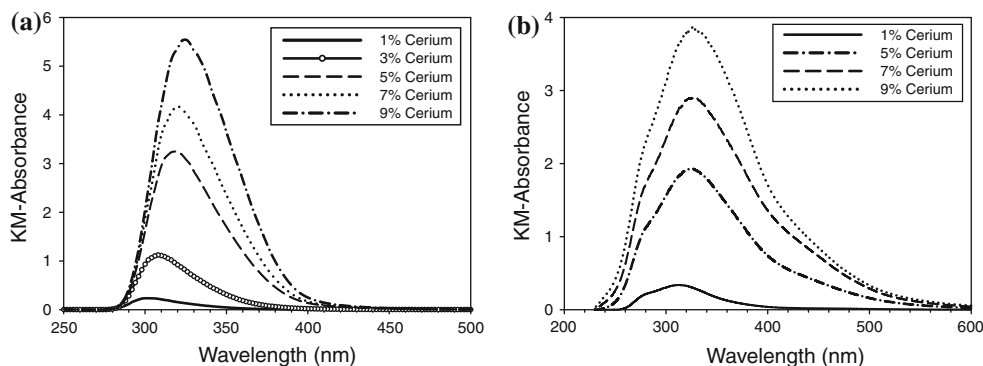
The areas of the absorption bands at 310 and 335 nm, Fig. 13b, grow linearly with the cerium concentration according with Lambert–Beer law with a R^2 of 0.995 and 0.978, respectively, supporting the above explanation.

On the other hand, fitting of UV–Visible spectra of cerium doped powders was resolved into four Gaussian bands (Fig. 14); their maxima being located at 277, 311, 348 and 423 nm. The band at 277 nm is assigned to Ce^{4+} and those at 311 and 348 nm correspond to Ce^{3+}, but

Fig. 11 AFM micrograph of coatings obtained from sols 1 day aged; **a** without Ce, **b** TME-SiO$_2$-1Ce, **c** TME-SiO$_2$-5Ce and **d** TME-SiO$_2$-9Ce
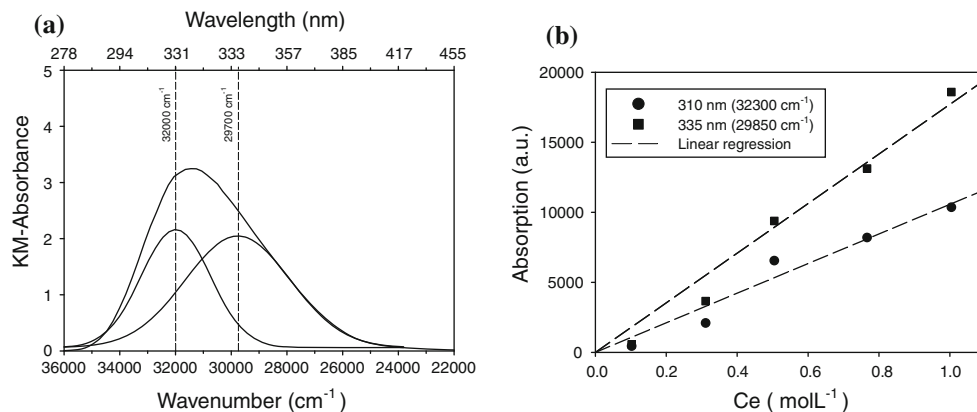

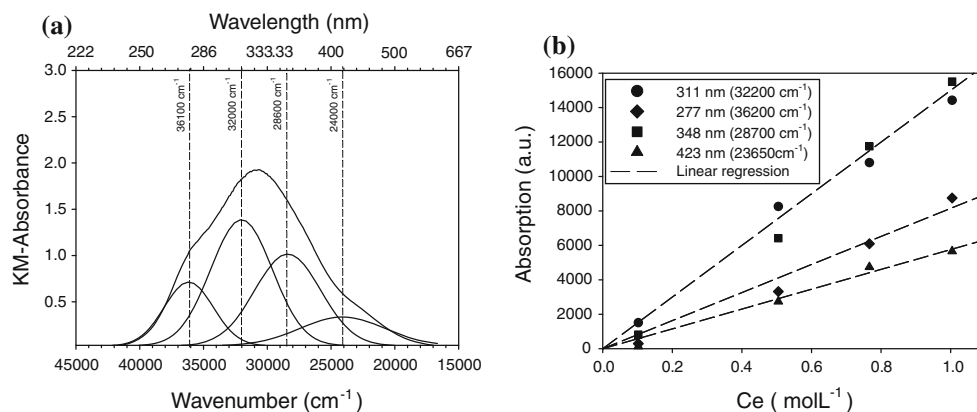**Fig. 12** UV–Vis spectra of Ce-doped coatings (**a**) and powder samples (**b**)

no reference has been found of a band centred at 423 nm. Taking into account the TEM and FE-SEM results in coatings with Ce-content higher than 3%, as well as previous literature in similar sol–gel processes, we could assign this band to colloidal Ce$_x$O$_y$ nanoparticles, which optical effects should be ruled by the Mie theory. The intensity and area of this band are much lower than those of Ce^{3+} and Ce^{4+}. However, an intense yellow colour is observed when this band increases supporting its identification with colloidal particles [44]. On the other hand, although the cerium precursor is in trivalent state and no significant oxidation is expected during sol–gel process, the

band corresponding to Ce^{4+} is considerable because the much higher molar absorptivity of charge transfer bands respecting to that of Ce^{3+} (5–10 times in glasses) [25, 32], since d-d transitions are formally forbidden by the Laporte rule. The areas of all the absorption bands follow a linear behaviour as a function of cerium concentration (Fig. 14b), according to Lambert–Beer and Mie laws. In all cases the value of R^2 is better than 0.995.

Figure 15 show the evolution of Ce^{4+}/Ce^{3+} ratio as a function of cerium concentration. The bands considered for calculating this ratio are that at 276 nm (Ce^{4+}) related to the addition of 310 and 348 nm bands of Ce^{3+}. The molar
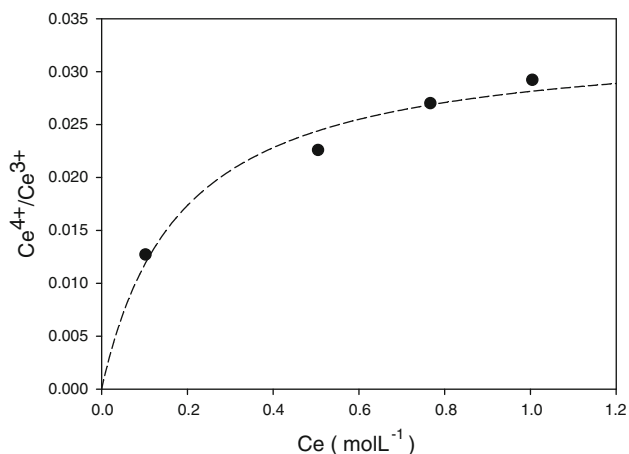
Fig. 13 a Deconvolution of UV–Visible spectra of 5% Ce-doped coatings and **b** Areas of the absorption at 310 and 335 nm bands as a function of cerium concentration

Fig. 14 a Deconvolution of UV–Visible spectra of 5% Ce-doped powder and **b** Areas of the absorption at 277, 311, 348 and 423 nm bands as a function of cerium concentration

absorptivity of Ce^{4+} has been approximated as 10 times that of Ce^{3+}, this providing a semi-quantitative figure of the evolution of redox states of cerium that shows a small but evident oxidation for increasing Ce-contents.

Fig. 15 Evolution of Ce^{4+}/Ce^{3+} ratio as a function cerium concentration

The difference observed in the redox behaviour of cerium ions in coatings and powders produced from the same sols can be explained taking into account the different processes used for obtaining the final materials. Coatings were obtained by dipping in which the film is a dried during extraction, "*frozen*" the liquid structure and its redox state. The thermal treatment at 120 °C is not enough to change the initial redox equilibrium. On the other hand, powders were obtained by drying and sintering during longer times, this permitting the slight change in the redox state and the precipitation of the colloidal Ce_xO_y nanoparticles.

In conclusion, we have shown the strong effect of cerium doping on hybrid organic–inorganic sol–gel sols, powders and coatings reinforced with colloidal silica nanoparticles. The viscosity of sols increases with cerium content; a maximum concentration of 5% mol of cerium is compatible with a stability of the sol of at least 100 h. The redox behaviour of cerium in powders and coatings is different. Coatings spectra present only Ce^{3+} bands, the yellow colour appearing for higher cerium contents being

likely explained by very small and scarce precipitated colloids, not solved in the UV spectra deconvolution. Instead, sol–gel powders present complex absorption bands with the presence of Ce^{4+}, Ce^{3+} and new band at 423 nm, assigned to Ce_xO_y colloids. Further additions of cerium produce both agglomeration and precipitation of Ce_xO_y amorphous nanoparticles, leading to a porous coating structure, with lower barrier properties. This compromise between maximum cerium concentration and enough stability of sols and coatings permits obtaining high cross-linking and organic polymerisation higher than 40%. TEM, FE-SEM and AFM confirmed this behaviour.

We have also proved that cerium is mainly as Ce^{3+} on Ce-containing coatings, this being suitable to facilitate the ion diffusion to damaged sites when applied onto metallic substrates, precipitating as Ce_xO_y oxides or hydroxides and promoting self-healing behaviour.

4 Conclusions

Coatings and powers have been produced from hybrid organic–inorganic sols with Ce concentrations up to 9% mol. The stability of the sols is greatly affected by Ce content as well the density and porous structure of the coatings developed from them.

The redox behaviour of cerium is different in powders and coatings. UV–Visible spectra show that Ce in coatings appears only as Ce^{3+} since the thermal treatment at 120 °C is not enough to change the redox equilibrium. Ce^{4+}, Ce^{3+} and a new band at 423 nm, assigned to Ce_xO_y colloids, have been assigned in sol–gel powders. Ce concentrations higher than 3% generate precipitation of Ce_xO_y amorphous colloids that confer a characteristic yellow colour to the coatings.

A compromise has been established between a maximum Ce content of 5% mol (TME-SiO$_2$-5Ce) with a sol stability of at least 100 h, this producing cross-linked coating structures with more than 40% of organic polymerisation.

References

1. Caglieri A, Goldoni M, Acampa O, Antreoli R, Vettori MV, Corradi M, Apostoli P, Mutti A (2006) Env Health Perspectives 114:542
2. Durán A, Castro Y, Aparicio M, Conde A, Damborenea JJ (2007) Int Mater Rev 52:175
3. Metroke TL, Gandhi JS, Apblett A (2004) Prog Org Coat 50:231
4. Metroke TL, Kachurina O, Knobbe ET (2002) Prog Org Coat 44:185
5. Liu Y, Sun D, You H, Chung JS (2005) Appl Surf Sci 246:82
6. Conde A, Durán A, Damborenea JJ (2003) Prog Org Coat 1273:1
7. Rosero-Navarro NC, Pellice SA, Castro Y, Aparicio M, Durán A (2009) Surf Coat Technol 203:1897
8. Rosero-Navarro NC, Pellice SA, Durán A, Ceré S, Aparicio M (2009) J Sol-Gel Sci Technol 52:31–40
9. Rosero-Navarro NC, Pellice SA, Durán A, Aparicio M (2008) Corr Sci 50:1283
10. Khramov AN, Voevodin NN, Balbyshev VN, Mantz RA (2005) Thin Solid Films 483:191
11. Moutarlier V, Neveu B, Gigandet MP (2008) Surf Coat Technol 202:2052
12. Zheludkevich M, Shchukin G, Yasakau KA, Möhwald H, Ferreira MGS (2007) Chem Mater 19:402
13. Palanivel V, Huang Y, Ooij WJ (2005) Prog Org Coat 53:153
14. Trabelsi W, Triki E, Dhouibi L, Ferreira MGS, Zheludkevich ML, Montemor F (2006) Surf Coat Technol 200:4240
15. Trabelsi W, Cecilio P, Ferreira MGS, Montemor F (2005) Prog Org Coat 54:276
16. Anatas PT, Williamson TC (1996) Green chemistry. American Chemical Society, Washington
17. Ho D, Brack N, Scully J, Markley T, Forsyth M, Hinton B (2006) J Electrochem Soc 153:B392
18. Birbilis N, Buchheit RG, Ho D, Forsyth M (2005) Electrochem Solid-State Lett 11:C180
19. Frutos A, Arenas MA, Liu Y, Skeldon P, Thompson GE, Damborenea JJ, Conde A (2008) Surf Coat Technol 202:3797
20. Sainz MA, Durán A, Fernández Navarro JM (1990) J Non-Cryst Solids 121:315
21. Aubonnet S, Perry C (2000) J Alloys Compd 300:224
22. Reisfeld R, Minti H, Patra A, Ganguli D, Gaft M (1998) Spectrochim Acta 54:2143
23. Reisfeld R, Hormodaly J (1972) J Chem Phys Lett 17:248
24. Huijuan B, Cai W, Zhang L (2000) Mater Res Bull 35:1495
25. Smith HL, Cohen AJ (1963) Phys Chem Glasses 4:173
26. Patra A, Kundu D, Ganguli D (1997) J Sol-Gel Sci Technol 9:65
27. Paul A, Mulholland M, Zaman MS (1976) J Mater Sci 11:2082
28. Reisfeld R, Patra A, Panczer G, Graft M (1999) Opt Mater 13:81
29. Jorgensen CK, Brinen J (1963) Research notes 629
30. Cano E, García MA, Villegas MA, Battaglin G, Llopis J, Bastidas JM (2001) Opt Mater 17:459
31. Krasôvec UO, Orel B, Sûrca A, Bukove N, Reisfeld R (1999) Solid State Ionics 118:195
32. Ishii Y, Arai K, Namikawa H, Tanaka M, Negishi A, Handa T (1987) J Am Ceram Soc 70:72
33. Fidalgo A, Ilharco LM (2001) J Non-Cryst Solids 283:144
34. Sassi Z, Bureau JC, Bakkali A (2002) Vip Spectroscopic 28:299
35. Chmel A, Mazurina EK, Shashkin VS (1990) J Non-Cryst Solids 122:285
36. Strawbridge I, James PF (1986) J Non-Cryst Solids 86:381
37. Guglielmi M, Zenezini S (1990) J Non-Cryst Solids 121:303
38. Pellice SA, Galliano P, Castro Y, Durán A (2003) J Sol-Gel Sci Technol 28:81
39. Wenzel RN (1936) Ind Eng Chem 28:988
40. Wolansky G, Marmur A (1999) Colloids Surf A 156:381
41. Liu YR et al (2007) Comp Sci Technol 67:2864
42. Almeida RM, Pantano CG (1990) J Appl Phys 68:4225
43. Gallardo J, Durán A, Martino D, Almeida RM (2002) J Non-Cryst Solids 298:219
44. Mennig M, Schmitt M, Schmidt H (1997) J Sol-Gel Sci Technol 8:1035